Metrology of thin layer deposition with combined XRR-GIXRF analysis at SOLEIL

Yves Ménesguen, Marie-Christine Lépy

Metrology of thin layer deposition with combined XRR-GIXRF analysis at SOLEIL synchotron

Y. Ménesguen[1] and M.-C. Lépy[1]

[1]Université Paris-Saclay, CEA, LIST, Laboratoire National Henri Becquerel (LNE-LNHB), F-91120 Palaiseau, France

X-ray reflectometry, spectrometry, grazing incidence X-ray fluorescence, thin films structure

Abstract

A new instrument called CASTOR is operated at the SOLEIL synchrotron facility and is dedicated to the characterization of thin films with thicknesses in the nanometer range. The instrument can combine X-ray reflectivity (XRR) measurements with fluorescence (XRF) acquisitions and especially total reflection X-ray fluorescence (TXRF) related techniques such as grazing incidence XRF (GIXRF). The instrument is now routinely installed on the hard X-ray branch of the Metrology beamline and reproducibility is studied as well as reference-free GIXRF analysis. Some representative examples are given to illustrate the capabilities of the setup and of the analysis.

1 Introduction

The multilayered thin film stacks with layer thicknesses in the nanometer range have been commonly characterized by X-ray reflectometry (XRR) on synchrotron facilities or with in-lab sources for years [1]. Reflectivity curves are acquired by varying the incident angle in the grazing incidence regime while recording the intensity of the specular reflected beam. Grazing incidence X-ray fluorescence (GIXRF) is a total reflection X-ray fluorescence analysis (TXRF) related technique [2], which uses the X-ray fluorescence (XRF) angle-dependent intensity at shallow incidence angles. The renewed interest for these techniques came from the elaboration of nanomaterials for applications in power electronics, electricity storage and microelectronics, which require new means of characterization. The XRF signal is element-specific and contains information about the elemental composition, concentration profiles and thicknesses. The combination of XRR, sensitive to the electronic density, and GIXRF, sensitive to element density, produces results of better accuracy compared to one technique alone. Some experimental facilities have already been developed to allow GIXRF-XRR combined analysis, using either synchrotron radiation [3, 4] or laboratory X-ray sources [5, 6].

The Laboratoire National Henri Becquerel (LNHB) acquired an instrument to perform such measurements at the Metrology beamline of the SOLEIL synchrotron source in order to propose metrological studies of thin film deposits to support the efforts of institutes or companies in the fast-developing field of nanolayered structures. The instrument CASTOR (Chambre d'Analyse Spectrométrique en Transmission ou en Réflexion) is a seven axis goniometer based on the model developed at the PTB and TU Berlin [3, 7].

This work describes the main part of the instrument and additional equipment, the experimental conditions at the Metrology beamline of the SOLEIL synchrotron facility and the first results obtained on selected samples.

2 Characteristics of the experimental setup

2.1 The hard X-ray branch at SOLEIL Metrology beamline

At the SOLEIL synchrotron (France), the hard X-ray branch monochromator device is composed of a double Si(111) crystal whose Bragg angle is equipped with a rotary position encoder that requires a calibration. The available energy range, defined by the extrema Bragg angles, is 3 to 45 keV. An accurate calibration of the energy axis of the monochromator is obtained by using several metal foils as transmission targets and energy scanning around their absorption edges. The first derivative of these transmission measurements is used to determine the accurate absorption edge energies which are compared to the ones tabulated in Deslattes [8], which finally allows to derive the corresponding angles using Bragg's law. The comparison with the absolute angles gives an offset that is provided to the monochromator device. The residual difference between the angular position given by the encoder and the values derived from the tabulated absorption edges is presented in [9] and is kept below 0.04%. The minimization of harmonics or stray light are managed in the same way as detailed in [9]. The contributions of the harmonics are significant below 7 keV and in these cases, a small detuning of the second monochromator crystal is necessary to reduce their total contribution to 0.1%.

2.2 Characteristics of the CASTOR experimental chamber

The CASTOR setup is a vacuum chamber equipped with a 7-axes manipulator. It is connected to the vacuum of the Metrology beamline for each measurement campaign and must be removed afterwards. That is the reason why it must be aligned prior to any experimental measurements. The most critical alignement being the coincidence between the vertical rotation axis and the beam path. Using a dedicated iterative procedure, the position of the CASTOR chamber perpendicular to the beam direction is defined by a motorized stage.

The internal manipulator of CASTOR is composed of seven axes with five motors for the sample and two dedicated to the detection arm (see Figure 1). The samples are placed vertically on two perpendicular translation stages (namely Tz and Ts) which are mounted on a rotation stage (Rx). This three-axis platform is attached on a horizontal translation stage (Tx) which is on the upper rotation stage (Rθ). The detection arm is on a second rotation stage (Rθ2). The fourth translation (Tz2) allows the detector to be selected. The Rθ and Rθ2 are the most critical axes for the experiments and are encoded for better accuracy. They can rotate freely except that collisions are prevented by a limit switch on the Rθ arm. This configuration allows the sample manipulator and the detector arm to rotate freely within the chamber. The rotation stage Rx has a range of 350°. The translation stages have 110 mm ranges except for Tx which is limited to 102 mm.

The detection arm Rθ2 is equipped with four photodiodes and an energy-dispersive detector (e.g., Silicon Drift Detector (SDD)). The photodiode holders can be equipped with commutable slits or collimators. The current configuration is composed of four 100 mm^2 photodiodes from Opto Diode [10, 11] that have a typical efficiency of 0.27 A/W within the photon energy range available at the beamline. In slot n°1, an AXUV:Al photodiode is equipped with a 300 µm vertical slit (used for alignment or measurements). The Al coating is necessary to prevent the infra-red or visible light degrading the dark current or background, improving the dynamic range of the reflectivity curves. Moreover, an AXUV100G photodiode equipped with no slit, placed in slot n°2, was absolutely calibrated using a cryogenic electrical-substitution radiometer [12].

A spectrometer such as an energy-dispersive detector is required to perform fluorescence-related measurements such as GIXRF. It is installed on the chamber facing the sample (i.e. at 90° with respect to the incoming beam.). The experiments are performed with an SDD from AMPTEK (128 eV of FWHM resolution at 5.9 keV), which is mounted on a dedicated translation stage allowing it to approach as close as possible to the sample.

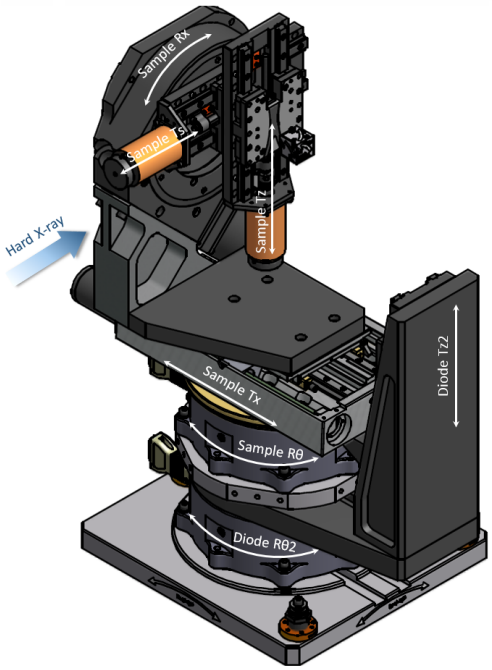

Figure 1: A schematic representation of the 7-axis goniometer. The beam is impinging the sample from the left, the surface of the sample being vertical.

3 X-ray fundamental parameters

The accuracy of reference-free GIXRF relies on the accuracy of atomic fundamental parameters such as the total mass attenuation coefficients (μ), the photoelectric cross sections (τ) and the fluorescence yields (ω). The XRR relies on the refractive index decrement (δ) and the absorption index (β) which are linked to the complex atomic scattering factor in forward direction ($f(0)$). The imaginary part of $f(0)$ can be directly calculated from the total mass attenuation coefficients and its real part is deduced from μ by thet Kramers-Kronig dispersion relation.

At LNHB, we performed absolute measurements of the total mass attenuation coefficients for various elements [9, 13] including a detailed evaluation of their associated uncertainties. This allows us to derive new values of optical indices consistent with mass attenuation coefficients and photoelectric cross sections used in the combined reference-free XRR-GIXRF analysis. We also developed a methodology to measure fluorescence yields, either from K shell [14] or partial fluorescence yields in the case of L shells [15, 16], but this work is less advanced and a more comprehensive database is still useful [17].

4 Experimental combined XRR-GIXRF analysis

4.1 Alignment and measurement procedure

The alignment of the CASTOR setup is crucial prior to any sample alignment. In this first step of the alignment procedure, the main goal is to make coincident the vertical axis of rotation of the sample holder with the path of the beam. For that purpose, we use a 200 µm diameter pinhole placed on the sample

holder to perform the scannings. The Tx translation stage (perpendicular to the beam when $\theta = 0°$ or 180°) is scanned to find the centre position of the beam within the pinhole for $\theta = 0°$. The same scan is performed for $\theta = 180°$ and the average between the two Tx positions gives the correct position for which the pivot is aligned with the beam. The whole chamber is moved according to this correction. We estimate the accuracy of the procedure to be in the range 10-20 µm due to the precision of the translation stage of the chamber.

The second important alignment step in the experiment concerns the samples. For each sample, we use a well-known approach. We repeatedly scan on Tx and Rθ until no change are found in the expected values with respect to the precision of the translation or rotation steps. With the translation stage Tx, we cut in half the incident beam intensity and by rotating the theta angle (rotation stage Rθ), we set the sample at the maximum intensity. Nevertheless, in order to verify the accuracy, we scan the rotation stage Rθ2 at a fixed θ angle (rocking curve) and record the photodiode current. If the maximum intensity is not exactly at $R\theta 2 = 2 \times R\theta$, a small theta offset is applied.

4.2 Solid angle of detection

A dedicated software to the CASTOR setup allows the user to acquire the X-ray fluorescence emitted by the sample simultaneously or sequentially with the X-ray reflectivity, in order to combine both XRR and GIXRF. In both cases some geometrical aspects are of importance to model correctly the sample in the fitting procedure. The footprint of the incoming beam on the sample is primarily defined by a slit. The samples being vertical, we use a vertical slit in order to limit the horizontal divergence of the beam and allow more flux by selecting larger height. We can use several slits of 100 µm width and 1, 3 or 5 mm vertical aperture.

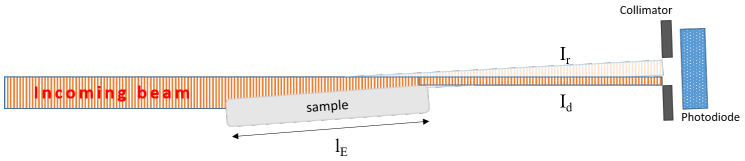

Figure 2: Geometry for the XRR at shallow angles.

In the case of the XRR, the theta scanning begins at 0°, for which the detected beam on the photodiode is the direct excitation beam cut in half. When increasing slowly the theta angle, the direct beam detection is progressively reduced (I_d on Fig. 2 left) and the reflected beam becomes dominant on the photodiode. The notch in the XRR close to 0.08-0.1° correspond to the moment when no further direct beam is detected on the photodiode. Its position and depth depend on the sample length (l_E), photodiode distance, collimator width and incoming beam width. All these geometrical effects are taken into account in our model.

The X-ray fluorescence signal is acquired by the SDD for which the geometrical aspects are of major importance (fig. 3). A tungsten collimator (thickness e and diameter c) is placed in front of the SDD and the distance to sample (d_1) can be adjusted manually. The solid angle is calculated accordingly to the measured distances and the dimensions of the collimator and the sample as well as the incoming beam characteristics (shape and dimensions). In a first step, we calculate the solid angle as a function of the radial distance r as every excited point on the sample will not contribute with the same importance to the signal of the SDD, as given in Equation 1:

$$\Omega_r(r) = \iint^{S(r)} \frac{sin(\beta)}{((d_1 + e + d_2)^2 + (r + x)^2 + y^2)} dxdy \tag{1}$$

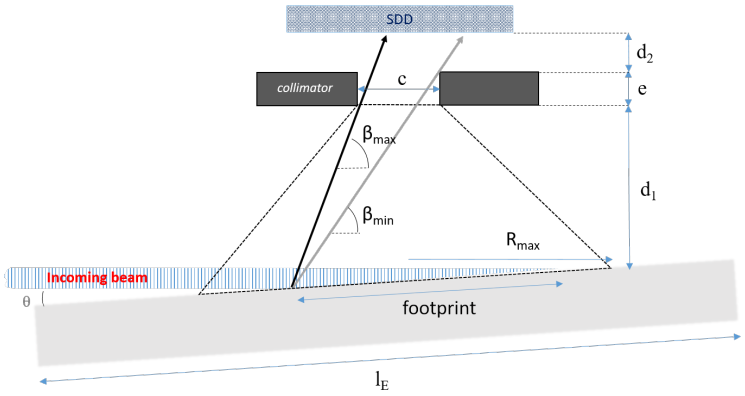

Figure 3: A schematic representation of the field of view of the SDD. The measured distances are indicated as they are used for the estimation of the solid angle.

where d_1 is the distance between the sample and the SDD collimator, e is the collimator thickness, d_2 is the distance between the collimator and the SDD silicon chip. The angle β is given by $\beta = arctan\left((d_1+e+d_2)/\sqrt{(r+x)^2+y^2}\right)$. The integral limits are expressed as a surface $S(r)$ which is the region common to several circles: $S(r) = A_{SDD} \wedge A_{c1} \wedge A_{c2}$, where A_{SDD} is the area of the SDD active area, A_{c1} and A_{c2} are the projected area on the SDD surface of the front and back side of the pinhole respectively. $\Omega_r(r)$ takes positive values for $0 \leq r \leq R_{max}$, R_{max} being the maximal off-axis distance.

In order to calculate the solid angle for every incident angle, the length of the sample (l_E) and the spot size of the beam are required. The following formula (Equation 2) is derived at each individual incident angle:

$$\Omega(\theta) = \frac{1}{A_s} \iint_{A_s} \Omega_r(r)\, dxdy \tag{2}$$

where A_s is the area in common of the impinging beam spot, the size of the sample and the field of view of the SDD delimited by the maximal radius R_{max}.

4.3 Simulation of the XRR

To simulate the x-ray reflectivity of any sample, we use the Parratt recursive formula [1] together with the Nevot-Croce formalism [18] to account for the interface roughness. At the Metrology beamline, the polarization is horizontal, the experiments will therefore be performed with P-polarization. At glancing angles (i.e. the very first points close to 0°), geometrical effects disturb the X-ray reflectivity. At 0°, half of the incoming flux is directly measured by the photodiode. The limited length of the sample prevent the measurement of the real reflection intensity for angles lower than $\sim 0.2°$. These geometrical effects are taken into account in our simulations. Our fitting procedure uses a differential method as in [19] with a χ^2 cost function of $XRR(\theta) \times \theta^5$.

4.4 Calculating the emitted x-ray fluorescence without any reference

To calculate the emitted fluorescence of a specific element from the sample, the evaluation starts with the calculation of the x-ray standing wave field inside the structure. The Parratt recursive algorithm gives the value of forward and backward electric fields at the centre of each layer. In order to take into account

the variation of the field and the interfaces roughnesses, our model cut the layers into thinner slabs. The detected fluorescence is derived using Equation 3:

$$\begin{aligned} XRF_i(\theta) &= \Omega(\theta) I_0 T \eta_i \tau_i \omega_i \times \sum_j \left[W_i(z_j)\rho(z_j)(z_j - z_{j-1}) \times \right. \\ &\left. \parallel E_t(z_j,\theta) + E_r(z_j,\theta) \parallel^2 \times exp(-\sum_{h=1}^{j-1} \mu_i(z_h)\rho(z_h)(z_h - z_{h-1})) \right] \end{aligned} \quad (3)$$

where T is the live time of each spectrum, I_0 is the flux of incident photons, η_i is the detector full energy peak efficiency at the line energy of element i, τ_i is the photoelectric cross sections of element i at incoming energy and ω_i the partial fluorescence yields of element i (corresponding to the shell fluorescence yields combined with the line ratio). In case the line is excited by several subshells due to the Coster-Kronig cascade, this has to be taken into account as well. The parameter $W_i(z_j)$ corresponds to the weight fraction of element i at depth z_j and $\rho(z_j)$ is the density at the same depth. The emitted fluorescence is reabsorbed when passing through the upper slabs and the exponential term in Equation 3 accounts for that. The solid angle $\Omega(\theta)$ must be calculated for each grazing angle as for the internal electric fields $E_t(z_j,\theta)$ and $E_r(z_j,\theta)$. To meet our experimental setup, we derived the calculation of the x-ray standing wave field for P polarization. Thus, the electric field is replaced by $H(z_j,\theta)/n$.

As for the x-ray reflectivity, the fitting parameters are the layer densities, thicknesses, roughnesses and elemental weight ratio. The combination of both the XRR and GIXRF techniques that are using similar measurement procedures but different signals provide better accuracy of these profiles.

4.5 Example of refence-free GIXRF analysis

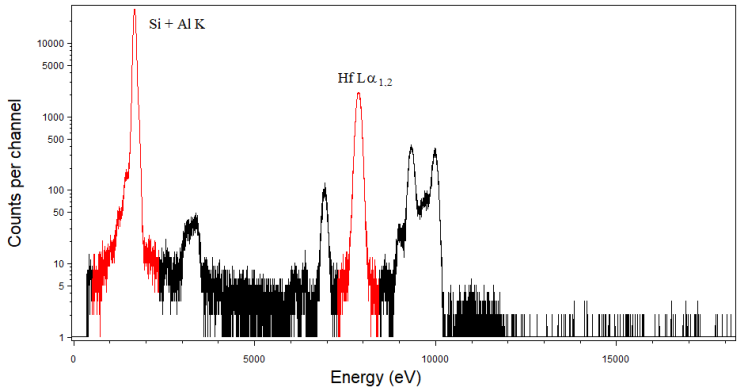

Figure 4: Right: Experimental x-ray fluorescence spectrum at 10 keV and $\theta = 0.32°$.

As an example of our approach, we performed a combined XRR/GIXRF analysis on a three-layered sample. The layers are $HfO_2/Al_2O_3/HfO_2$ deposited by atomic layer deposition (ALD) on Si substrate. The incoming photons with an energy of 10 keV create vacancies in the K shell of aluminum, silicon and oxygen and in the L_3shell of hafnium, avoiding any Coster-Kronig transitions. The SDD is set at $d_1 =$ 15 mm and the incoming beam was cut at 0.1x0.5 mm. We acquired 149 spectra of 150 s from 0° to 3°, of which we derived the hafnium $L\alpha$ line area at every angular step. The spectra are processed using the COLEGRAM software [20] to get the peak areas, using Gaussian functions (Fig. 4). The background of all spectra were processed to take into account the step due to the presence of a peak. As $L\alpha_2$ could not be distinguished from $L\alpha_1$, the derived peak areas account for both line contributions. The experimental curves are presented in Figure 5. On the left, we compare the acquired XRR with the simulation and, on the

	This work (ng.mm^{-2})	PTB in [21]	LETI in [21]
HfO_2	11.7	6.8(10)	13.6(19)
Al_2O_3	9.1	10.3(16)	11.1(8)

Table 1: Comparison of areal mass derived for different experiments. In this work, we used the combined GIXRF-XRR analysis, as PTB and LETI used XRR.

centre, we compare the experimental Hf $L\alpha$ line intensity with the result of the GIXRF calculation following our model. The excellent agreement between all experimental and theoretical curves gives confidence in the reliability of the parameters of the structure. In Figure 5 right, we give an overview of the depth-dependent densities derived by our model.

This sample was already studied in [21] by the same techniques but with different apparatus and excitation energies. The three-layered sample corresponds to the S2 sample of the article. In the published analysis, the HfO_2 and Al_2O_3deposited materials were assumed to be stoichiometric and having bulk density, 9.68 g.cm^{-3} and 3.95 g.cm^{-3}for HfO_2 and Al_2O_3 respectively, which is not our case since significantly lower densities derived from our fit. In order to compare our results with the ones published in [21], we derive the areal mass for HfO_2 and $Al_2O_3$from the layer densities and thicknesses and we present the results of [21] in Table 1 together with our results. Our result are in good agreement for Al_2O_3 with PTB and LETI, nevertheless a lower content maybe due to the difficulty to distinguish the aluminum $K\alpha$ line from the large tail of the silicon $K\alpha$ peak (we cannot excite at photon energy lower than 3 keV on the hard X-ray branch, thus the silicon peak being very intense). Our result concerning $HfO_2$are in better agreement with LETI and significantly different from PTB.

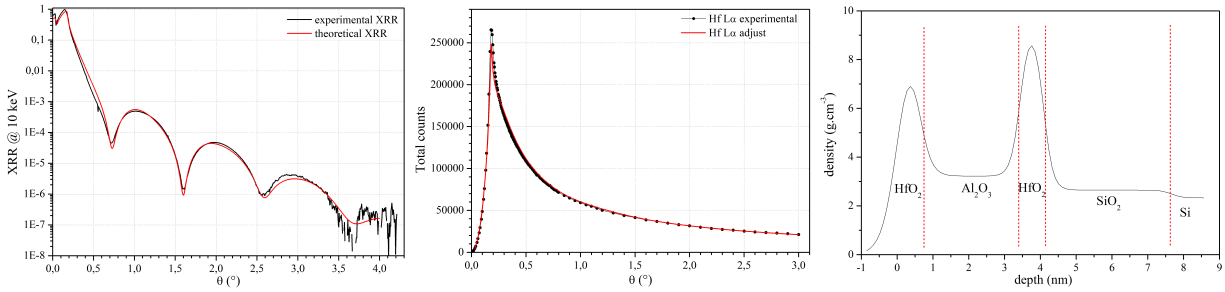

Figure 5: Left: Experimental and theoretical XRR at 10 keV. Centre: GIXRF plot of Hf $L\alpha$ line. Right: Fitted density from air to silicon substrate (right).

5 Conclusion

We presented a combined XRR-GIXRF analysis of several samples. At first, we assessed our measurement procedure and calculation method on a well-known sample in different conditions in order to qualify our instrument and theoretical work. Then, we applied our procedure to more complex samples in order to derive their interesting quantities. We found an excellent agreement between experimental results and fitted curves of both XRR and GIXRF which supports the confidence in the stack parametres derived.

Acknowledgements

The authors are grateful to Pascal Mercere and Paulo Da Silva for assistance on the Metrology beamline and to the SOLEIL staff for smoothly running the facility and to Emmanuel Nolot and Diane Eichert for fruitful discussion.

References

[1] L. G. Parratt, "Surface Studies of Solids by Total Reflection of X-Rays," *Physical Review*, vol. 95, no. 2, pp. 359–369, 1954.

[2] D. K. G. de Boer, "Glancing-incidence x-ray fluorescence of layered materials," *Physical Review B*, vol. 44, no. 2, pp. 498–511, 1991.

[3] J. Lubeck, B. Beckhoff, R. Fliegauf, I. Holfelder, P. Hönicke, M. Müller, B. Pollakowski, F. Reinhardt, and J. Weser, "A novel instrument for quantitative nanoanalytics involving complementary X-ray methodologies," *Review of Scientific Instruments*, vol. 84, p. 045106, 2013.

[4] G. Das, S. R. Kane, K. Ajay, A. K. Singh, and M. K. Tiwari, "Simultaneous measurement of X-ray reflectivity and grazing incidence fluorescence at BL-16 beamline of Indus-2," *Review of Scientific Instruments*, vol. 86, p. 055102, 2015.

[5] D. Ingerle, M. Schiebl, C. Streli, and P. Wobrauschek, "Combination of grazing incidence x-ray fluorescence with x-ray reflectivity in one table-top spectrometer for improved characterization of thin layer and implants on/in silicon wafers," *Review of Scientific Instruments*, vol. 85, p. 083110, 2014.

[6] M. Spanier, C. Herzog, D. Grötzsch, F. Kramer, I. Mantouvalou, J. Lubeck, J. Weser, C. Streeck, W. Malzer, B. Beckhoff, and B. Kanngiesser, "A flexible setup for angle-resolved X-ray fluorescence spectrometry with laboratory sources," *Review of Sc*, vol. 87, p. 035108, 2016.

[7] J. Lubeck, M. Bogovac, B. Boyer, B. Detlefs, D. Eichert, R. Fliegauf, D. Grötzsch, I. Holfelder, P. Hönicke, W. Jark, R. B. Kaiser, B. Kanngießer, A. G. Karydas, J. J. Leani, M. C. Lépy, L. Lühl, Y. Ménesguen, A. Migliori, M. Müller, B. Pollakowski, M. Spanier, H. Sghaier, G. Ulm, J. Weser, and B. Beckhoff, "A new generation of x-ray spectrometry UHV instruments at the SR facilities BESSY II, ELETTRA and SOLEIL," *AIP Conference Proceedings*, vol. 1741, p. 030011, 2016.

[8] R. D. Deslattes, E. G. Kessler, P. Indelicato, L. de Billy, E. Lindroth, and J. Anton, "X-ray transition energies: new approach to a comprehensive evaluation," *Reviews of Modern Physics*, vol. 75, no. 1, pp. 35–99, 2003.

[9] Y. Ménesguen, M. Gerlach, B. Pollakowski, R. Unterumsberger, M. Haschke, B. Beckhoff, and M.-C. Lépy, "High accuracy experimental determination of copper and zinc mass attenuation coefficients in the 100 eV to 30 keV photon energy range," *Metrologia*, vol. 53, pp. 7–17, 2016.

[10] Opto Diode Corporation (US). [Online]. Available: http://optodiode.com/

[11] R. Korde, C. Prince, D. Cunningham, R. E. Vest, and E. Gullikson, "Present status of radiometric quality silicon photodiodes," *Metrologia*, vol. 40, pp. S145–S149, 2003.

[12] P. Troussel and N. Coron, "BOLUX: a cryogenic electrical-substitution radiometer as high accuracy detector in the 150-11000 eV range," *Nuclear Instruments & Methods in Physics Research, Section A: Accelerators, Spectrometers, Detectors, and Associated Equipment*, vol. 614, pp. 260–270, 2010.

[13] Y. Ménesguen, M.-C. Lépy, P. Hönicke, M. Müller, R. Unterumsberger, B. Beckhoff, J. Hoszowska, J.-Cl. Dousse, W. Błachucki, Y. Ito, M. Yamashita, and S. Fukushima, "Experimental determination of the x-ray atomic fundamental parameters of nickel," *Metrologia*, vol. 55, pp. 56–66, 2018.

[14] Y. Ménesguen and M.-C. Lépy, "Mass attenuation coefficients in the range $3.8 \leq E \leq 11$ kev, K fluorescence yield and K_β/K_α relative X-ray emission rate for Ti, V, Fe, Co, Ni, Cu, and Zn measured with a tunable monochromatic X-ray source," *Nuclear Instruments & Methods In Physics Research B*, vol. 268, no. 16, pp. 2477–2486, 2010.

[15] J. M. Sampaio, T. I. Madeira, J. P. Marques, F. Parente, A. M. Costa, P. Indelicato, J. P. Santos, M.-C. Lépy, and Y. Ménesguen, "Approaches for theoretical and experimental determinations of K-shell decay rates and fluorescence yields in Ge," *Physical Review A*, vol. 89, p. 012512, 2014.

[16] Y. Ménesguen and M.-C. Lépy, "Experimental determination of L fluorescence yields of gadolinium," *X-Ray Spectrometry*, 2020.

[17] M. O. Krause, "Atomic Radiative and Radiationless Yields for K and L Shells," *Journal of Physical and Chemical Reference Data*, vol. 8, no. 2, pp. 307–328, 1979.

[18] L. Névot and P. Croce, "Caractérisation des surfaces par réflexion rasante de rayons X. Application à l'étude du polissage de quelques verres silicates," *Revue de Physique Appliquée*, vol. 15, pp. 761–779, mars 1980.

[19] G. Ingerle, D.and Pepponi, F. Meirer, P. Wobrauschek, and C. Streli, "JGIXA - A software package for the calculation and fitting of grazing indcidence X-ray fluorescence and X-ray reflectivity data for the characterization of nanometer-layers and ultra-shallow-implants," *Spectrochimica Acta, Part B: Atomic Spectroscopy*, vol. 118, pp. 20–28, 2016.

[20] H. Ruellan, M.-C. Lépy, M. Etcheverry, J. Plagnard, and J. Morel, "A new spectra processing code applied to the analysis of ^{235}U and ^{238}U in the 60-200kev energy range," *Nuclear Instruments & Methods In Physics Research A*, vol. 369, pp. 651–656, 1996.

[21] P. Hönicke, B. Detlefs, M. Müller, E. Darlatt, E. Nolot, H. Grampeix, and B. Beckhoff, "Reference-free, depth-dependent characterization of nanolayers and gradient systems with advanced grazing incidence X-ray fluorescence analysis," *Physica Status Solidi A*, vol. 212, no. 3, pp. 523–528, 2015.